Fault tolerant multi-sensor data fusion for autonomous navigation in future civil aviation operations

S. Ifqir, C. Combastel, A. Zolghadri, G. Alcalay, P. Goupil, S. Merlet

Version of Record: https://www.sciencedirect.com/science/article/pii/S0967066122000454
Manuscript_f6c0e80b7627bb281a1d934d43c1ed37

Fault tolerant multi-sensor data fusion for autonomous navigation in future civil aviation operations

S. Ifqir[a,*], C. Combastel[a], A. Zolghadri[a], G. Alcalay[b], P. Goupil[b], S. Merlet[b]

[a] *IMS Lab, University of Bordeaux - CNRS 33405 Talence, France*
[b] *Airbus Operations S.A.S. - St. Martin, 316 route de Bayonne, 31060 Toulouse, France*

Abstract

The problem addressed in this paper is that of fault-tolerant multi-sensor data-fusion for flight navigation during approach and landing of a civil jetliner. The work falls within the scope of a large collaborative project on future single pilot operations issues. The proposed methodology is based on a multi-layer hierarchical architecture which can integrate several heterogeneous information sources. The study is restricted to three classical information sources, namely, Inertial Reference System (IRS), Global Positioning System (GPS) and Instrument Landing System (ILS). The system is designed to meet the specified navigation performance requirements in terms of validity, accuracy, continuity and on-board implementation issues. The methodology takes advantage of recently developed set-membership tools, and paves the way toward a new and simple tuning of global merging filter.

Keywords: Multi-sensor data fusion; Fault tolerance, Autonomous navigation, Civil aircraft.

*Corresponding author
Email addresses: sara.ifqir@ims-bordeaux.fr (S. Ifqir), christophe.combastel@ims-bordeaux.fr (C. Combastel), ali.zolghadri@ims-bordeaux.fr (A. Zolghadri), guillaume.alcalay@airbus.com (G. Alcalay), philippe.goupil@airbus.com (P. Goupil), samuel.merlet@airbus.com (S. Merlet)

Nomenclature

SPO	Single Pilot Operations.
IRS	Inertial Reference System.
GPS	Global Positioning System.
ILS	Instrument Landing System.
ENU	East-North-Up.
NWD	North-West-Down.
QFU	Magnetic bearing of the runway in use.
GMF	Global Merging Filter.
SMA	Self-Monitoring Algorithm.
CIC	Confidence Interval Computation
CST	Coordinate System Transformation.
V&V	Verification and Validation.

1. Introduction

1.1. Context

In civil aviation operations, the trend is pointed toward more autonomy and intelligence in the cockpit. The next leap forward is to take one pilot out of the cockpit (SPO: Single Pilot Operation, 2030+) [1, 2]. Future SPO cockpit avionics must provide specific functionalities [3]. Autonomous navigation is one of the required technological advances identified by the aviation sector to achieve the long term, the multiples and challenging goals toward more autonomous aircraft. Aircraft navigation system performance requirements are often measured in terms of accuracy, integrity, continuity and availability, see for instance [4].

This paper deals with navigation issues in next generation SPO, where the onborad coordinated crews will no longer be available as a resource, compared to status quo. The paper focuses on the approach and landing phases and provides a flexible architecture and algorithms for fault-tolerant multi-sensor data fusion. The system is intended to integrate several sources of (heterogeneous) information to enhance the performance of in-service navigation systems, and to

assist the single pilot in correctly managing common and extreme flights circumstances. The work falls within the scope of an ongoing large French collaborative project focused on new technologies for future intelligent cockpit[1].

1.2. Today state of practice

Current navigation trends include integrated navigation systems where the sensors typically integrated are Inertial Navigation/Reference System (INS/IRS) and the Global Positioning System (GPS), see for instance [5]. The idea behind the (INS/IRS)/GPS integration stems from the fact that although the two subsystems produce the same outputs, 3D position and velocity, they measure different quantities and are subject to different kinds of error/faults or unavailability conditions and issues. While an INS/IRS system estimates position and velocity by measuring acceleration and angular rate and then integrating these quantities to generate the output, the GPS directly measures position and velocity. Many research papers exist on (INS/IRS)/GPS fusion for navigation among others, see for example [5, 6] and the references therein. However, the performance of the integrated system is still limited by GPS satellite navigation availability [7]. Therefore, additional data from other different sensors have to be integrated with the (INS/IRS)/GPS existent solution to provide an accurate and reliable measurement. In recent years, vision-based landing systems have been extensively investigated [8, 9, 10]. Although the proposed algorithms have made remarkable progress in vision-assisted landing navigation, the real-time performance may be still limited because of constrained computational resources. Moreover, when fused with other sensors, the vision-based measurements can be inevitably subject to a non negligible time-delay (due to the image processing computational time). Moreover, poor visibility may also impact the measurements. Unlike vision-based landing systems, Instrument Landing Systems (ILS) has served as standard tool in commercial aircraft since the end of the '60s. The ILS provides both lateral and vertical guidance for alignment (LOC:

[1] See `http://ali-zolghadri.com/the-kom-of-cocotier-project/`.

Localizer) and descent (GS: Glide Slope) of an aircraft approaching and landing on a runway, even in poor weather conditions and reduced visibility. ILS also has a number of basic limitations, for example ILS has insufficient accuracy (due to the propagation characteristics associated with the transmission frequencies involved) and landing in low visibility conditions requires ILS CAT II/III infrastructures that represent a significant investment. Recently, Ground-Based Augmentation System (GBAS) has been considered as an effective alternative to the existing ILS and has been approved to meet the requirements of Category I operations [11]. However, due to its total dependence on GPS, GBAS is very sensitive to interference and jamming. In addition, not all aircraft are equipped with GBAS capabilities, therefore, airports will need to maintain their ILS infrastructure which have to be augmented with complementary systems to provide an accurate and continuous navigation solution.

However, most of the current state-of-the art works in the field of aircraft final approach and landing navigation do not address the integration of the ground-based instrument system ILS in their data fusion scheme. By contrast with such studies e.g. focusing on INS/GPS integrated approaches [12], vision-aided and optical relative navigation [13, 14, 15], or INS/GPS augmentation through a radar altimeter [16, 17], this paper proposes a new IRS/GPS/ILS fault-tolerant multi-sensor data fusion algorithm. The integration is performed using Kalman filtering [18]. Nevertheless, as the major difficulty in designing Kalman filters for sensor fusion is the incomplete prior information about the noise covariance matrices [19], a new and simple tuning procedure taking advantage from some recently developed set-membership tools is proposed. To the best of the authors' knowledge, only a preliminary study on the integration of GPS, ILS and vision-based measurements with IMU acceleration and rate gyro has been proposed in [9]. However, no monitoring mechanism or updates of the noise covariance matrices have been reported in this context. Finally, it should be underlined that this work extends the authors' preliminary study presented in [20] on several important aspects including the monitoring layer and validation on real flight data.

1.3. Problem statement and related contributions

In this paper, a multi-layered, modular, flexible and dynamically configurable fault-tolerant data fusion architecture is presented. The design and implementation are intended to provide reliable aircraft position (in three dimensions) by fusing measurements from IRS, GPS and ILS. The overall architecture is depicted in Figure 1. Each layer has a processing task and a given structure that contributes to the overall data fusion process. The lower level (layer 0) of the proposed architecture is called Preprocessing Layer. It acquires data from involved sensors groups and performs preprocessing and/or common referencing of incoming heterogeneous data to obtain comparable measurements. The Layer 1, called First-Level Signal Verification Layer, performs sensor signal extraction and characterization based on recently developed set-membership tools. In Layer 2, monitoring and signal behaviour validity analysis is performed. Layer 3 fuses data from multiple valid and fault-free sensors, and combines them into more reliable, concise and consistent solution. Applying the proposed architecture to IRS/GPS/ILS integrated navigation system results in an efficient and effective data fusion algorithm.

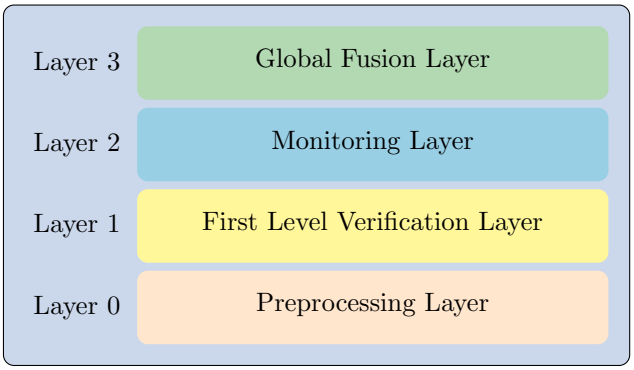

Figure 1: Four-level architecture.

The paper is organized as follows: Section 2 describes the proposed Four-layered architecture. Section 3 discusses how IRS/GPS/ILS fusion is operated within the proposed architecture. The effectiveness of the proposed method-

ology is demonstrated in Section 4 using real flight data. Finally, concluding remarks including directions for future works are drawn in Section 5.

2. System Overview

As already outlined, a Four-layered architecture is adopted in this paper, see Figure 2. The main processing at each layer is described below.

Layer 0 - Preprocessing Layer. In the lowest layer, data collected from a common fault-free reference sensor and n auxiliary distributed sensors groups are preprocessed. Since the objective of this level is to provide Layer 1 with consistent information, all observations from different available sensors are mapped to a common reference frame using a Coordinate System Transformation (CST).

Layer 1 - First-Level Signal Verification Layer. This layer mainly focuses on feature extraction from each single preprocessed data. A basic learned/tuned model characterizing the range of admissible physical behaviors of incoming data is proposed. This characterization is used to define some important parameter settings in the upper layers, and in particular, the noise covariance matrices.

Layer 2 - Monitoring Layer. This layer implements real-time self-monitoring algorithms that are configured to evaluate whether sensors present valid or invalid behaviors. When a source is declared to be invalid, it is excluded from further processing. However, once the sensor returns to its normal operating condition, and restores validity, it is automatically reintegrated into the data fusion process.

Layer 3 - Global Fusion Layer. In this layer, all valid and fault-free data from multiple sources is fused to obtain a more precise estimate. In this paper, a Kalman filtering based-fusion algorithm is used to combine a state prediction with the available measurements. However, given the modular aspect of the proposed multi-layer architecture, other filtering techniques modules could be also integrated.

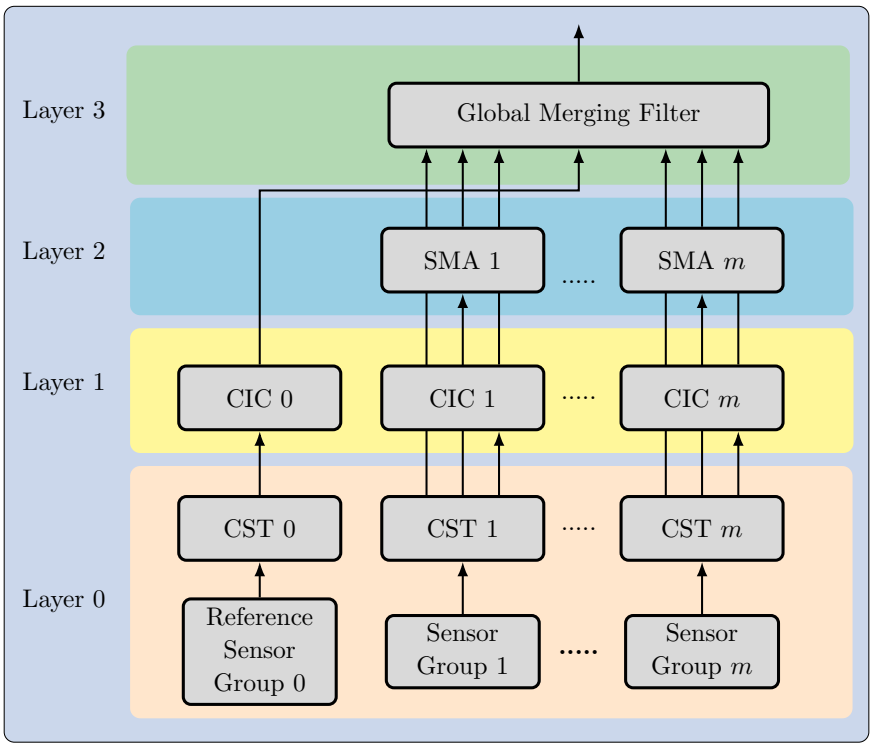

Figure 2: Illustration of the Four-layered architecture for fault tolerant multi-sensor data fusion (CST: Coordinate System Transformation, SMA: Self-Monitoring Algorithm, CIC: Confidence Interval Computation).

3. IRS/GPS/ILS integrated navigation system

In this section, the proposed general architecture is applied to perform IRS/GPS/ILS fault-tolerant data fusion, i.e. $m = 3$. IRS is considered as the common fault-free reference sensor, GPS and ILS are the auxiliary group sensors. The index $i \in \{0, 1, 2\}$ is used in the rest of the paper to refer to IRS, GPS and ILS sensor groups, respectively. The j-th observation of the i-th sensor group is noted as y_{ij}, $i \in \{1, \ldots, m\}$ and $j \in \{1, \ldots, m_i\}$.

Note that, IRS information is assumed to have been processed and consolidated on-board using a dedicated triplex monitoring system. IRS outputs can also be further consolidated using other redundant on-board information. This

issue is not investigated in this paper but notice that an appropriate decision test can provide information on when and how a source moves away from a reference (see for instance [21]).

In the following, after the description of each layer, the considered coordinate frames are introduced. Then, a method for evaluating the prediction of measurements confidence intervals is proposed. Afterwards, the validity of sensor data is evaluated. Finally, the measurements models and filtering used in the integration process are developed.

3.1. Layer 0

In this layer, the original real-time measurements provided by sensor groups IRS and GPS are collected and expressed in a common locally-fixed runway frame. The latter is defined as a frame fixed to the runway with its origin located at the middle of the runway threshold. ILS output measurements are directly expressed with respect to the runway frame and are not concerned by the following preprocessing procedure. In what follows, reference frames used in this paper are briefly described; Transformations between them are reported in Appendix A. Then, available IRS and GPS measurements are expressed with respect to the runway frame before being conveyed to the upper layer.

3.1.1. Coordinate frames

WGS84 - Earth centered, Earth fixed ellipsoidal coordinate system (o-frame). The World Geodetic System - 1984 (WGS 84) coordinate system is a Conventional Terrestrial System (CTS) widely used in GPS-based navigation [22]. Its origin is fixed to the Earth's center of mass and characterizes a coordinate point near the earth's surface in terms of latitude (ϕ), longitude (λ), and height (h). An illustration of an aircraft latitude and longitude is given in Figure 3.

Earth-Centered, Earth-Fixed Cartesian frame (e-frame). The ECEF frame uses three-dimensional XYZ coordinates (in meters) to describe the location of a GPS user or satellite. The term "Earth-Centered" comes from the fact that the origin of the axis $(0, 0, 0)$ is located at the center of the Earth (See Figure 3). The term

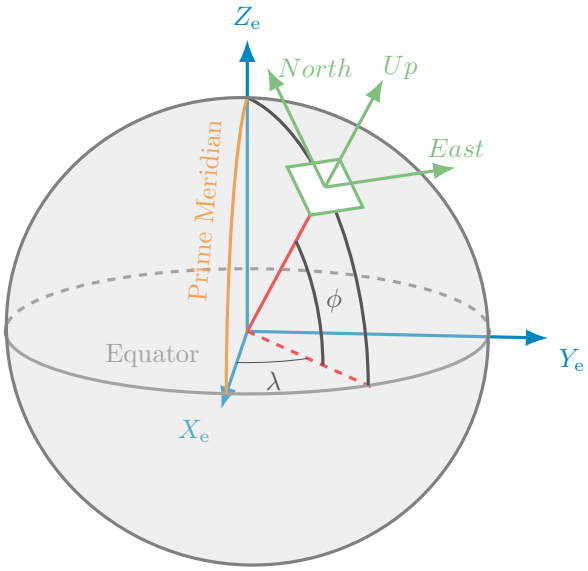

Figure 3: Coordinate and reference frames

"Earth-Fixed" implies that the axes are fixed with respect to the earth (that is, they rotate with the earth). The X-axis points to the intersection between the Equator and the Prime meridian (latitude 0°, longitude 0°), the Y-axis points to 0° latitude and 90°E longitude and the Z-axis points to the North Pole (latitude 90° N along the axis of rotation of the Earth).

East-North-Up frame (ENU-frame or u-frame). Its origin coincides with the intersection of the runway threshold and center line. The x-axis points East in the local parallel direction and the y-axis points North in the local meridian direction. Z-axis is pointing up and completes a right-handed coordinate system.

Runway Coordinate System (r-frame). In our application, the r-frame is locally fixed to the runway on which the aircraft is approaching. Its origin is located at an intersection of the runway threshold and center-line. The X-axis lies along the runway center-line direction pointing towards the approach direction. The Z-axis points downward and the Y-axis points leftward to complete the left-hand rule used consistently with the available models and data.

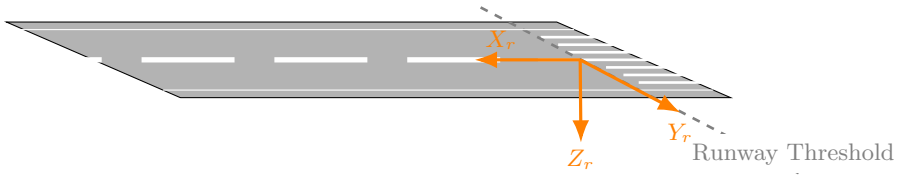

Figure 4: Runway Frame.

3.1.2. Coordinate System Transformation

IRS system provides aircraft three-dimensional velocity in the local ENU navigation frame. At time instant k, let $y_0^r[k]$ be the IRS measurements expressed with respect to the runway frame:

$$y_0^r[k] = \begin{bmatrix} V_{X_0}^r[k] \\ V_{Y_0}^r[k] \\ V_{Z_0}^r[k] \end{bmatrix} \tag{1}$$

where $V_{X_0}^r[k]$, $V_{Y_0}^r[k]$ and $V_{Z_0}^r[k]$ represent aircraft velocity along x-, y- and z-axis. Then, the required transformation is calculated as follows:

$$y_0^r[k] = C_u^r \begin{bmatrix} V_{X_0}^u[k] \\ V_{Y_0}^u[k] \\ V_{Z_0}^u[k] \end{bmatrix} \tag{2}$$

where C_u^r, given in (A.5), is the transformation matrix relating the u-frame and runway frame.

On the other hand, the GPS receiver provides the aircraft's position in o-frame as a latitude, longitude, and height. Converting coordinates from o-frame to runway frame (r-frame) is not possible through a single rotation matrix. First, the latitude, longitude and height coordinates must be converted to Earth-Center-Earth-Fixed coordinates and then expressed in the local navigation u-frame before being given with respect to the runway frame. In this regard, define $y_1^r[k]$ to be the GPS three-dimensional position observations at time instant k

with respect to the runway frame as

$$y_1^r[k] = \begin{bmatrix} X_1^r[k] \\ Y_1^r[k] \\ Z_1^r[k] \end{bmatrix} \tag{3}$$

where $X_1^r[k]$, $Y_1^r[k]$ and $Z_1^r[k]$ represent position along x-, y- and z-axis. Then, GPS measurement vector y_1^r is calculated according to the following equation:

$$y_1^r[k] = C_u^r \, C_e^u \left(\begin{bmatrix} X_1^e[k] \\ Y_1^e[k] \\ Z_1^e[k] \end{bmatrix} - \begin{bmatrix} X_{RWY}^e[k] \\ Y_{RWY}^e[k] \\ Z_{RWY}^e[k] \end{bmatrix} \right) \tag{4}$$

where $(X_1^e[k],\ Y_1^e[k]\ Z_1^e[k])$ is GPS position in e-frame calculated from GPS geodetic coordinates ($\phi_1[k]$, $\lambda_1[k]$, $h_1[k]$) using Equations (A.2) as follows:

$$\begin{bmatrix} X_1^e[k] \\ Y_1^e[k] \\ Z_1^e[k] \end{bmatrix} = \begin{bmatrix} \left(\frac{a_e}{\sqrt{1-e^2 sin^2(\phi_1)}} + h_1[k] \right) cos(\phi_1[k]) cos(\lambda_1[k]) \\ \left(\frac{a_e}{\sqrt{1-e^2 sin^2(\phi_1)}} + h_1[k] \right) cos(\phi_1[k]) sin(\lambda_1[k]) \\ \left(\frac{a_e(1-e^2)}{\sqrt{1-e^2 sin^2(\phi_1)}} + h_1[k] \right) sin(\phi_1[k]) \end{bmatrix} \tag{5}$$

where a_e and e stand for the earth semi-major axis and the eccentricity, respectively. The origin position of u-frame expressed in e-frame is calculated from geodetic coordinates ($\phi_{RWY}[k]$, $\lambda_{RWY}[k]$, $h_{RWY}[k]$) provided by the runway database as

$$\begin{bmatrix} X_{RWY}^e[k] \\ Y_{RWY}^e[k] \\ Z_{RWY}^e[k] \end{bmatrix} = \begin{bmatrix} \left(\frac{a_e}{\sqrt{1-e^2 sin^2(\phi_{RWY})}} + h_{RWY}[k] \right) cos(\phi_{RWY}[k]) cos(\lambda_{RWY}[k]) \\ \left(\frac{a_e}{\sqrt{1-e^2 sin^2(\phi_{RWY})}} + h_{RWY}[k] \right) cos(\phi_{RWY}[k]) sin(\lambda_{RWY}[k]) \\ \left(\frac{a_e(1-e^2)}{\sqrt{1-e^2 sin^2(\phi_{RWY})}} + h_{RWY}[k] \right) sin(\phi_{RWY}[k]) \end{bmatrix} \tag{6}$$

C_e^u is the transformation matrix that rotates a vector from the e-frame to local navigation frame (u-frame). Its components are computed in terms of runway threshold latitude and longitude using (A.4).

3.2. Layer 1

IRS, GPS, and ILS raw measurements are corrupted by noise during the acquisition process. One can view these signals as being the sum of a noiseless

yet physically consistent signal to be recovered, say $x^r_{ij}[k]$, and an undesired unknown but bounded additive noise $\omega_{ij}[k] \in \Omega$. Hence, one can write each scalar measurement signal as

$$y^r_{ij}[k] = x^r_{ij}[k] + f_{ij}\omega_{ij}[k], \;\; \omega_{ij} \in \Omega, \; \forall i, \; \forall j \tag{7}$$

where f_{ij} is the noise magnitude parameter and $\Omega \subset \mathbb{R}$ is an unitary interval box domain, i.e. $\Omega = [-1, \; 1]$.

An estimate of the component of interest $x^r_{ij}[k]$ can be obtained by filtering out the noise ω_{ij} from the noisy observation $y^r_{ij}[k]$. Using a causal, first-order, low pass IIR (Infinite Impulse Response) filter which has the following difference equation,

$$x^r_{ij}[k+1] = a_{ij}x^r_{ij}[k] + (1 - a_{ij})y^r_{ij}[k], \; \forall i, \; \forall j \tag{8}$$

a simple dynamical model of the desired signal physical behavior is obtained. It can be easily computed from the available data. However, it should be emphasized that the parameters f_{ij} and $0 < a_{ij} < 1$ in (7-8) are actually unknown and have to be identified. To that purpose, an offline data-driven identification schema can be used. The availability of fault-free flight historical data covering the normal operating ranges of each scalar measured value y^r_{ij} is assumed. The parameter a_{ij} is set based on temporal or frequential identification. Afterwards, the parameter f_{ij} viewed as the total (or maximum) absolute value (or magnitude) of the deviations (or errors) between measured and desired data, is derived as

$$f_{ij} = max(|y^r_{ij}[k] - x^r_{ij}[k]|), \; \forall i, \; \forall j \tag{9}$$

Now, using the equivalence shown in Figure 5, the equations in (7) and (8) can be, alternatively, written in a model-driven form as:

$$x^r_{ij}[k+1] = x^r_{ij}[k] + e_{ij}\omega_{ij}[k], \quad \forall i, \; \forall j \tag{10a}$$

$$y^r_{ij}[k] = x^r_{ij}[k] + f_{ij}\omega_{ij}[k], \; \forall i, \; \forall j \tag{10b}$$

where $e_{ij} = (1 - a_{ij})f_{ij}$. Clearly, since the noise vector $\omega_{ij}[k]$ is unknown but bounded, the exact estimation of the desired component $x^r_{ij}[k]$ cannot be

derived. A simple approach is to characterize the set of all admissible values consistent both with the prediction model (10) and online acquired measurement $y_{ij}^r[k]$.

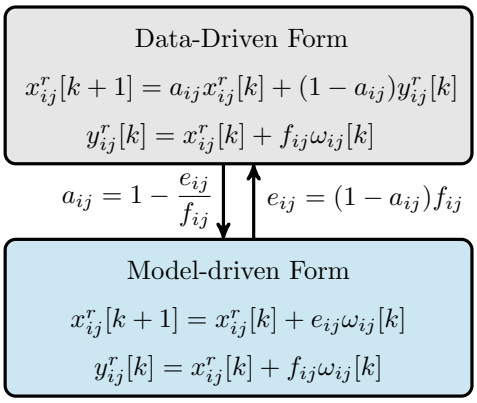

Figure 5: Equivalence between two forms of 1st order signal modeling.

In the sequel, a computationally efficient first order interval-based algorithm is proposed. At each sample time, a predicted set is calculated for each sensor elementary output y_{ij}^r. The basic structure is inspired by the Zonotopic Kalman Filter (ZKF) first proposed in [23] and further extended in [24]. By reducing first order zonotopes to intervals by changing the norm used to formulate the estimation accuracy optimization criterion, the adopted approach provides significant simplifications compared to generic n-dimensional zonotope-based algorithms. The resulting strategy is made possible without sacrificing accuracy in the considered scalar case, to the benefit of an easy implementation satisfying stringent real-time constraints.

Let $c_{ij}[k]$ and $r_{ij}[k]$ be the center and the radius of the confidence predicted interval enclosing the state $x_{ij}^r[k]$. The structure of the proposed first order interval-based method is introduced in the following proposition.

Proposition 1. Given the first order model (10), assume that the initial state $x_{ij}^r[0]$ belongs to the interval set with center $c_{ij}[0]$ and radius $r_{ij}[0]$. Then, the system

$$c_{ij}[k+1] = \gamma_{ij}[k]c_{ij}[k] + (1-\gamma_{ij}[k])y_{ij}^r[k],\ \forall i,\ \forall j \tag{11a}$$

$$r_{ij}[k+1] = pos(|y^r_{ij}[k] - c_{ij}[k]| - f_{ij}) + a_{ij}.min(r_{ij}[k], f_{ij}),\ \forall i,\ \forall j \qquad (11b)$$

where $pos(x) = x$ if $x > 0$ and 0 otherwise and $\gamma_{ij}[k] = a_{ij}$ if $r_{ij}[k] < f_{ij}$ and 0 otherwise, is a confidence interval predictor for (10) with a center $c_{ij}[k]$ and radius $r_{ij}[k]$ such that

$$x^r_{ij}[k] \in (c_{ij}[k] \pm r_{ij}[k]) = \left[\underline{x}^r_{ij}[k],\quad \overline{x}^r_{ij}[k]\right],\ \forall i,\ \forall j \qquad (12)$$

Furthermore, upper and lower bounds of the output $y^r_{ij}[k]$ are:

$$\begin{aligned} \underline{y}^r_{ij}[k] &= \underline{x}^r_{ij}[k] - f_{ij} \\ \overline{y}^r_{ij}[k] &= \overline{x}^r_{ij}[k] + f_{ij} \end{aligned} \qquad (13)$$

Proof. By introducing a correction gain g_{ij}, the Equation (10) becomes

$$x^r_{ij}[k+1] \quad = \quad x^r_{ij}[k] + e_{ij}\omega_{ij}[k] + g_{ij}[k](y^r_{ij}[k] - x^r_{ij}[k] - f_{ij}\omega_{ij}[k]) \qquad (14)$$

Recursively define the interval center and radius estimates $c_{ij}[k]$ and $r_{ij}[k]$ as:

$$c_{ij}[k+1] = (1 - g_{ij}[k])c_{ij}[k] + g_{ij}[k]y^r_{ij}[k] \qquad (15a)$$

$$r_{ij}[k+1] = \left|(1 - g_{ij}[k])r_{ij}[k]\right| + \left|(e_{ij} - g_{ij}[k]f_{ij})\right| \qquad (15b)$$

Note that Equations (15) can be tuned using a set size criterion. In fact, an optimal gain $g^*_{ij}[k]$ minimizing the uncertainty about $x^r_{ij}[k]$ can be deduced by minimizing the radius $r_{ij}[k]$ of the resulted confidence interval. By replacing e_{ij} in the radius recursive Equation (15), we get:

$$r_{ij}[k+1] = \left|(1 - g_{ij}[k])r_{ij}[k]\right| + \left|(1 - a_{ij} - g_{ij}[k])f_{ij}\right| \qquad (16)$$

The optimal gain $g^*_{ij}[k] = argmin\|r_{ij}[k+1](g_{ij}[k])\|_1$ minimizing the criterion $J_{ij}[k] = \|r_{ij}[k+1](g_{ij}[k])\|_1 = |1 - g_{ij}[k]|.|r_{ij}[k]| + |1 - a_{ij} - g_{ij}[k]|.|f_{ij}|$ can be computed by solving a simple l_1-norm Optimization Problem. An explicit

solution is obtained through a simple analysis of the variations of $J_{ij}[k]$ with regard to $g_{ij}[k]$:

$$\begin{aligned} J^*_{ij}[k] &= a_{ij}\ min(r_{ij}[k], f_{ij}) \\ g^*_{ij}[k] &= 1 - \gamma_{ij}[k] \end{aligned} \tag{17}$$

where $\gamma_{ij}[k] = a_{ij}$ if $r_{ij}[k] < f_{ij}$ and 0 otherwise. Then, by substituting the optimal gain $g^*_{ij}[k]$ for $g_{ij}[k]$ in (15a), (11a) is obtained. Furthermore, as $\|r_{ij}[k+1](g_{ij}[k])\|_1 = J_{ij}[k]$, the radius dynamics in (11b) is directly deduced using $J^*_{ij}[k]$. It should be underlined that, the term $pos(|y^r_{ij}[k] - c_{ij}[k]| - f)$ is added into (11b) in order to reconfigure the filter in case of inconsistency detection. When $|y^r_{ij}[k] - c_{ij}[k]| > f_{ij}$, i.e. $y^r_{ij}[k] \neq [\underline{y}^r_{ij}[k],\ \overline{y}^r_{ij}[k]]$ at time k, the predicted interval is automatically adjusted to encompass the new measurement data at the next time instant $k+1$ by enlarging the radius $r_{ij}[k+1]$. This reconfiguration makes it possible to restore the validity of the interval estimate with the underlying physical model of the sensed (and observed) signal immediately after the detection of an inconsistency. □

The complete interval predictor design process using iterative function is summarized in Algorithm 1.

Remark. To illustrate the filter reconfiguration, Figure 6 represents a signal that undergoes sudden changes in amplitude. Once $|y^r_{ij}[k] - c_{ij}[k]| - f_{ij} > 0$, the filter expands the upper and lower bounds to encompass the signal and preserve validity and consistency with signal physical behavior. Another benefit is that large uncertainties are naturally less weighted by Kalman filtering updates in upper layers of the architecture, which is consistent with the passivation of inconsistent/invalid signals.

3.3. Layer 2

This layer is deployed to monitor auxiliary sensor groups and determine whether the incoming data meet the fusion requirements in terms of validity. Each incoming data is associated with a measurement Validity Index, VI. This qualitative information is generated using a single bit, indicating whether the measurement is "valid", i.e $VI = 1$ or invalid, i.e. $VI = 0$.

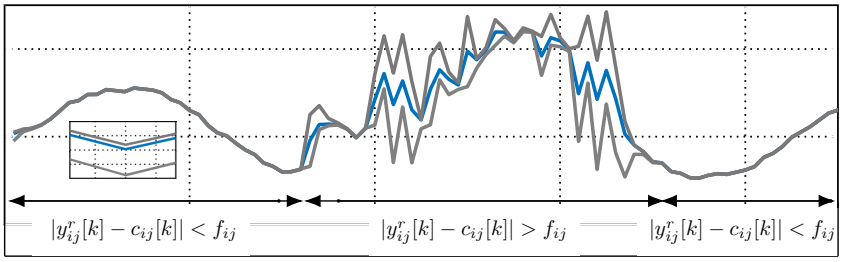

Figure 6: Illustration of predicted interval adjustment.

3.3.1. GPS Monitoring Module

In this section, a residual-based test is used for GPS abrupt fault detection and exclusion. An estimation of GPS measurement signal is obtained using a first-order filter with an innovation saturation mechanism. In fact, the proposed solution contains a sliding mode term, signum of the innovation process:

$$\hat{x}_{1j}[k+1] = \hat{x}_{1j}[k] + k_j.sign(y^r_{1j}[k] - \hat{x}_{1j}[k]), \quad \forall j \tag{18}$$

where k_j is a constant gain, $sign$ stands to the signum function and $\hat{x}_{1j}[k]$ is the estimation at time instant k of the GPS j-th observation $y^r_{1j}[k]$. The advantage of such a filter is that the innovation error $(y^r_{1j}[k] - \hat{x}_{1j}[k])$ is saturated when it is unreasonably large. This can reduce the effects of abrupt faults on the estimation error. The estimated value and the actual GPS output are then compared to acquire the residual signal $\mathcal{R}_{1j}$:

$$\mathcal{R}_{1j}[k] = y^r_{1j}[k] - \hat{x}_{1j}[k] \tag{19}$$

The chosen decision rule used to test the residual $\mathcal{R}_{1j}$ relies on a simple-moving RMS (Root Mean Square) analysis. This method expresses the energy content of the residual signal and provides a convenient measure of the magnitude evolution. The RMS value at sampling instant k, within a sliding window of length N, is calculated as follows:

$$RMS_{1j}[k] = \sqrt{\frac{1}{N}\left(\sum_{l=k-N+1}^{k} \mathcal{R}^2_{1j}[k]\right)} \tag{20}$$

The validity index $VI_{1j}[k]$, associated with the j-th observation $y^r_{1j}[k]$, is then generated by comparing the RMS value against a predefined threshold T_{1j} such that:

$$VI_{1j}[k] = \begin{cases} 0, \text{ if } RMS_{1j}[k] > T_{1j} \\ 1, \text{ if } RMS_{1j}[k] \leq T_{1j} \end{cases} \tag{21}$$

The detection threshold T_{1j} is set as the maximum influence of uncertainties on the residual signal and can be empirically determined using fault-free historical data.

3.3.2. ILS Monitoring Module

The Instrument Landing System (ILS) is a standard radio navigation aid used for guiding aircraft during the approach and landing. The ILS system consists of two radio beams, a Localizer (LOC) beam that provides horizontal guidance along the extended center-line of the runway and a Glideslope (GS) beam that provides vertical guidance toward the runway touchdown point. Deviations from the desired descent trajectory are measured through the amplitude difference between two modulated radio beams (at $90Hz$ and $150Hz$, respectively), called Difference in depth of modulation (DDM) [25]. The DDM is expected to be zero along the vertical and horizontal planes, defined by Glideslope and Localizer subsystems, and to vary linearly over a predefined angular sector on either side of the planes.

It is important that any failure/inconsistency in the ILS can be immediately detected. GS and LOC are valid only when used within a predefined strict boundaries and no fault has been detected. The overall workflow of the proposed ILS monitoring module is shown in Figure 7. In the first stage, the collected ILS signals are processed through appropriately designed pre-filters. In the second stage, two local monitoring algorithms are implemented in order to confirm the validity and accuracy of the data. A detection logic that collects the output indicators of each block provides a single bit, VI_2, that indicates whether the ILS measurements are valid or not.

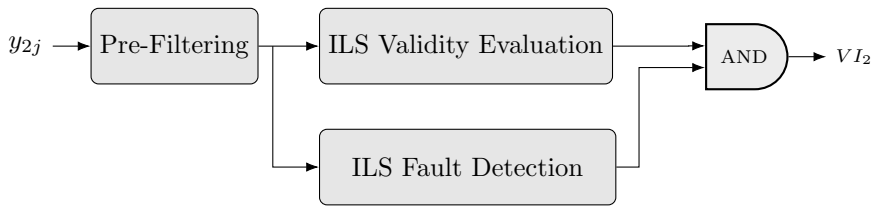

Figure 7: ILS Monitoring Architecture.

ILS Validity Evaluation. The criteria used to assess ILS validity is based on i) the longitudinal distance to the runway threshold [2], ii) DDM linearity region and iii) aircraft relative bearing such that:

- Localizer (resp. Glideslope) radiates usable signals up to a maximum distance of 80 (resp. 10) nautical miles (NM) from the runway threshold.
- DDM linearity is valid only within an operating range of ± 0.155 DDM (i.e $\pm 150 \mu A$) for Localizer and a range of ± 0.22 DDM for Glideslope.
- Relative bearing $\vartheta_r = QFU - \vartheta$ does not exceed 30 degrees for both Localizer and Glideslope. This angle is computed using the magnetic bearing of the runway in use, QFU, and the aircraft bearing ϑ defined as the angle of the aircraft forward direction from a line pointing to magnetic north as shown in Figure 8.

When received Glideslope (resp. Localizer) signal is outside of the advertised limits, the Glideslope (resp. Localizer) is judged to be invalid and inoperative and VI_2 is set to zero. Otherwise, unless a fault is detected, it is considered valid, i.e. $VI_2 = 1$.

ILS faults detection. The proposed scheme relies on signal time derivative estimation and evaluation. The time derivative is generated using a first-order

[2] Aircraft longitudinal position with respect to the runway is assumed to be available and provided by an on-board Air Data Inertial Reference Unit (ADIRU).

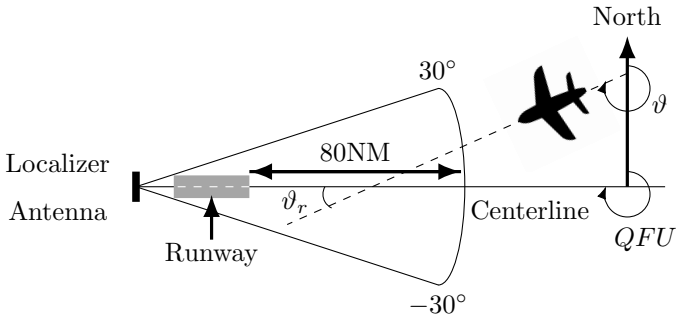

Figure 8: Aerial view of Localizer.

sliding mode differentiator, as proposed in [26]:

$$\begin{cases} \dot{z}_{2j}^0 = -\alpha_j^0 |z_{2j}^0 - y_{2j}^r|^{\frac{1}{2}} sign(z_{2j}^0 - y_{2j}^r) + z_{2j}^1 \\ \dot{z}_{2j}^1 = -\alpha_j^1 sign(z_{2j}^1 - \dot{z}_{2j}^0) = -\alpha_j^1 sign(z_{2j}^0 - y_{2j}^r) \end{cases} \tag{22}$$

where z_{2j}^0 is the estimate of the input signal y_{2j}^r and z_{2j}^1 is the estimate of its first derivative. The coefficients α_j^0 and α_j^1 are positive gains representing the adjustment parameters of the differentiator. These parameters ensure finite time convergence of the algorithm and vary as a function of the Lipschitz constant L, according to:

$$\alpha_j^0 = 1.5 L_j^{\frac{1}{2}} \, , \alpha_j^1 = 1.1 L_j \tag{23}$$

The value of the Lipschitz constant L_j is chosen so as to minimize the estimation error $|z_{2j}^0 - y_{2j}^r|$, $\forall j$. One of the advantages of the differentiator (22) is the reduced number of input parameters, i.e, a single setting parameter L_j. The discrete-time implementation of the differentiator (22) is based on the Forward Euler discretization method. The decision making stage involves an identical process as in the previous section. However, it should be noticed that other decision making strategies such as statistical decision theory or Narendra-type residual evaluation filter [27] can also be used.

3.3.3. Exclusion/Inclusion procedure

Let define a validity signature matrix $S[k] = blockdiag(S_1[k], S_2[k])$, where $S_1[k]$ and $S_2[k]$ are square matrices related to GPS and ILS, respectively. When,

the validity index associated with the i-th sensor, i.e. $VI_i[k]$, returns 0, the signature matrix is null, and the corresponding sensor signal is excluded from the global data fusion process until the index $VI_{ij}[k]$ comes back to the value one, e.g. $S_i[k] = I_{m_i}$.

3.4. Layer 3

IRS/GPS/ILS fusion algorithm based on Kalman filtering [28] is explained in this section. The following paragraphs will describe how each of these sensor groups is modeled in the global merging filter.

State model. The state vector, $x^r[k] \in \mathbb{R}^n$, to be estimated consists of aircraft three-dimensional position, along x-, y- and z-axis, i.e. $n = 3$,

$$x^r[k] = \begin{bmatrix} X^r[k], & Y^r[k], & Z^r[k] \end{bmatrix}^T \tag{24}$$

which may be modelled as:

$$x^r[k+1] = x^r[k] + T_s\left(y_0^r[k] - b_0[k]\right) \tag{25}$$

where T_s is the sampling period and $y_0^r[k]$ is the k-th IRS velocity measurement assumed to be corrupted by a bias $b_0[k]$ to be estimated. Every bias component in (25) is modeled as a random walk process,

$$b_0[k+1] = b_0[k] + \omega_b[k] \tag{26}$$

where $\omega_b[k]$ is zero mean Gaussian noise with covariance matrix Q_b. Employing a state augmentation schema, the state evolution model in (25) is extended with the random walk process model in (26) such that both the state and bias can be estimated simultaneously. Thus, the augmented state vector $\tilde{x}^r[k] = \begin{bmatrix} x^r[k], & b_0[k] \end{bmatrix}^T$ is governed by (27),

$$\tilde{x}^r[k+1] = \underbrace{\begin{bmatrix} I_n & -T_s I_n \\ 0_n & I_n \end{bmatrix}}_{\tilde{A}_0} \tilde{x}^r[k] + \underbrace{\begin{bmatrix} T_s I_n \\ 0_n \end{bmatrix}}_{\tilde{B}_0} c_0[k] + \underbrace{\begin{bmatrix} E_0[k] & 0_n \\ 0_n & E_b \end{bmatrix}}_{\tilde{E}_0[k]} \underbrace{\begin{bmatrix} \omega_0[k] \\ \omega_b[k] \end{bmatrix}}_{\tilde{\omega}_0[k]} \tag{27}$$

where $c_0[k]$ is the IRS speed signal estimated from the measurement $y_0^r[k]$ by the first-level verification layer (Layer 1) and $\omega_0[k]$ is a normal distributed noise. $E_0[k]$ is a time-varying matrix characterizing the IRS measurement noise, and E_b is a constant matrix related to the covariance matrix Q_b as $Q_b = E_b E_b^T$. In this work, $E_0[k]$ and E_b are kept diagonal.

Observation model. The GPS sensor returns aircraft three-dimensional position expressed in the runway frame. ILS provides vertical and horizontal angular deviations. The GS deviation signal is generated thanks to the antennas by reflecting a signal on the runway and must pass through a specific point called Threshold Crossing Height (TCH), which is usually $50ft$ beyond the runway threshold. An illustration of ILS GlideSlope beam is given in Figure 9. In this representation, aircraft altitude is determined using the Glide Path Angle (GPA $\approx 3°$) and the Threshold Crossing Height retrieved from the navigation database:

$$Z^r[k] = TCH - X^r[k]\, tan(GPA + \eta_{GS}^r[k]) \tag{28}$$

where $\eta_{GS}[k]$ is the GS deviation in degree which can be deduced using Equation (28) as follows:

$$\eta_{GS}^r[k] = tan^{-1}\left(\frac{TCH - Z^r[k]}{X^r[k]}\right) - GPA \tag{29}$$

The Localizer signal is generated from the ILS antenna which may not be exactly aligned with the runway. The aircraft relative lateral distance to the runway is

$$Y^r[k] = Y_{LOC}[k] + (L - X^r[k])\, sin(b_{align}) + d_{offset} \tag{30}$$

where b_{align} and d_{offset} are two constant offset values, and $Y_{LOC}[k]$ represents the lateral distance to the LOC signal as depicted in the Figure 10:

$$Y_{LOC}[k] = \eta_{LOC}[k]\, \frac{L - X^r[k]}{L} \tag{31}$$

$\eta_{LOC}[k]$ is the Localiser deviation in μA, s is the Localiser sensitivity (usually $0.7m/\mu A$) and L is the runway length (usually $3500m$).

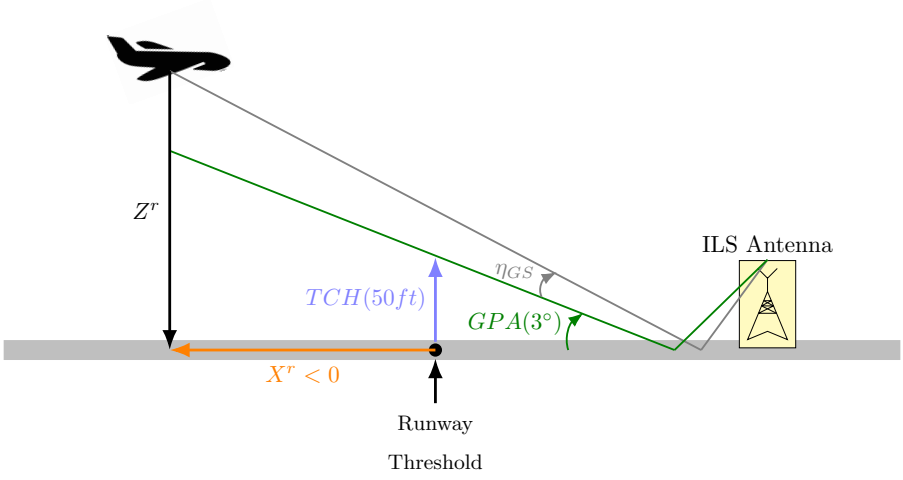

Figure 9: ILS Glideslope representation.

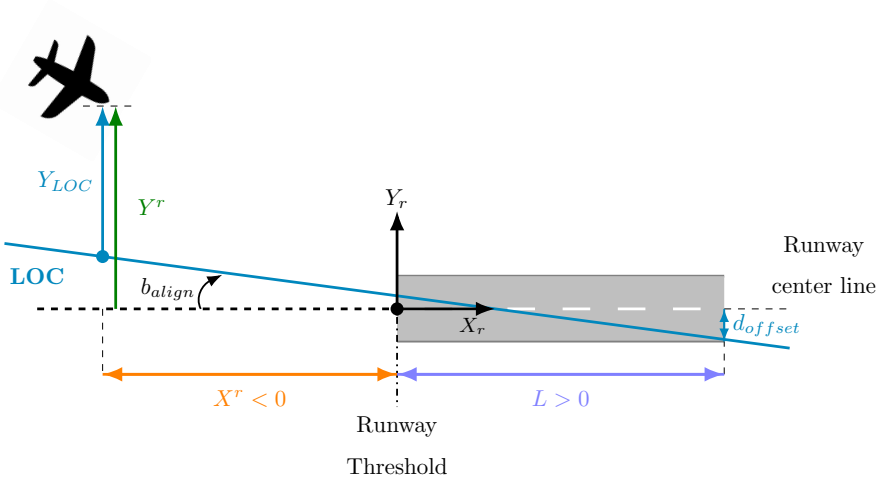

Figure 10: Position relative to the runway.

The processed GPS and ILS observations at each time are, therefore, described according to the following model:

$$y^r[k] = \begin{bmatrix} y_1^r[k] \\ y_2^r[k] \end{bmatrix} = h(\tilde{x}^r[k]) + \begin{bmatrix} F_1[k] & 0 \\ 0 & F_2[k] \end{bmatrix} \begin{bmatrix} \vartheta_1[k] \\ \vartheta_2[k] \end{bmatrix} \tag{32}$$

where $F_1[k]$ and $F_2[k]$ characterize GPS and ILS measurement noise $\vartheta_1[k]$ and $\vartheta_2[k]$. The nonlinear observation function $h(\tilde{x}^r[k])$ is given by

$$h(\tilde{x}^r[k]) = \begin{pmatrix} X^r[k] \\ Y^r[k] \\ Z^r[k] \\ \frac{\left(Y^r[k] - d_{offset} - (L - X^r[k])sin(b_{align})\right) L}{s(L - X^r[k])} \\ tan^{-1}\left(\frac{TCH - Z^r[k]}{X^r[k]}\right) - GPA \end{pmatrix} \tag{33}$$

IRS/GPS/ILS integration. Since the measurement equation (33) is non-linear, an Extended Kalman Filter (EKF) algorithm is used. Given an initial state estimate, $\hat{\tilde{x}}^r[0]$ and an initial state error covariance matrix, $P[0]$, the prediction-update scheme is applied recursively at each time step. The complete set of EKF recursive equations is given in Algorithm 2. The superscript (p) denotes predicted (prior) estimates. $H[k]$ is the Jacobian matrix of $h(.)$ obtained by linearizing around the updated state estimate $\hat{\tilde{x}}^r[k]$:

$$H[k] = \frac{\partial h}{\partial x}\Big|_{\hat{\tilde{x}}^r[k]} \tag{34}$$

$R[k]$ is a block diagonal matrix whose block diagonal components are GPS and ILS noise covariance matrices $R_1[k]$ and $R_2[k]$. The validity signature matrix $S[k]$ is computed following the procedure described in Subsection 3.3. The values of $R_1[k]$, $R_2[k]$ and IRS noise covarinace matricx $Q_0[k]$, are deduced later. Note that for final implementation, the EKF can be replaced by a multi-dimensional extension of Stirling's interpolation formula [29, 30] which does not require derivatives, but only functions evaluations. In general, this formulation will accommodate easier implementation than the EKF, since the differentiability of the nonlinear mappings is not required.

Tuning of the filter. The performance of Kalman filtering technique significantly depends on the covariance matrices of the process and measurement noise. In practice, these matrices are rarely known a priori and it is necessary to approximate them using available data and/or measurements. In this paper, the

modelling of the noise covariance matrices takes advantage of the proposed innovative interval techniques (cf. Subsection 3.2), which pave the way for an online and simple tuning of the filters.

Note that, data confidence interval computed in Subsection 3.2 characterizes signal error margins. In fact, for a given confidence level κ, the derived confidence interval for the observation $z_i^r[k]$ takes the form $\Big[\left(c_i[k] - \kappa\sigma_i\right),\ \left(c_i[k] + \kappa\sigma_i\right)\Big]$, where σ_i represents the vector of standard deviation of the i-th sensor and $c_i[k]$ is the center of the confidence interval (i.e nominal observation). This representation can be rewritten as $\Big[\left(c_i[k] - (r_i[k] + f_i)\right),\ \left(c_i[k] + (r_i[k] + f_i)\right)\Big]$ where the confidence interval center $c_i[k]$ and $(r_i[k] + f_i)$ serve as an estimate of the mean and the confidence radius for the i-th sensor dataset. Furthermore, by assuming that $\omega_0[k]$, $\vartheta_1[k]$ and $\vartheta_2[k]$ are independent, the associated covariance matrices are diagonal. The covariance matrices $Q_0[k]$, $R_1[k]$ and $R_2[k]$ are then computed respectively by using the positive semi-definite matrices $E_0[k] = diag(\frac{r_0[k]+f_0}{\kappa})$, $F_1[k] = diag(\frac{r_1[k]+f_1}{\kappa})$ and $F_2[k] = diag(\frac{r_2[k]+f_2}{\kappa})$ such that, $Q_0[k] = E_0[k]E_0^T[k]$, $R_1[k] = F_1[k]F_1^T[k]$ and $R_2[k] = F_2[k]F_2[k]^T$. It should be emphasized that the resulting noise covariance matrices are adaptive as they depend on the time-varying radius $r_i[k]$. When the noise on the sensor measurement increases, or if it changes drastically, the interval radius widens, and the noise covariance matrix increases accordingly.

4. Results

This section is devoted to assess the effectiveness of the proposed fault tolerant multi-sensor data fusion methodology. The four-layered architecture in Figure 1 is integrated into a dedicated development/validation simulation tool provided by AIRBUS. The objective of this platform is to provide a simulation environment in order to facilitate test, development and V&V tasks. The environment allows the user to perform Monte Carlo simulations from a set of flight test files consisting of several aircraft approach and landing manoeuvres. The user can specify potential failures affecting the input variables of the algorithm.

The simulation tool is developed within MATLAB/SIMULINK environment.
In what follows, four landing scenarios have been selected. The 3D trajectories plots of the flight profiles are illustrated in Figure 11. Figure 12 shows projections of the landing trajectories on the x-y and x-z planes. The sampling frequency for all recorded data is $16Hz$.

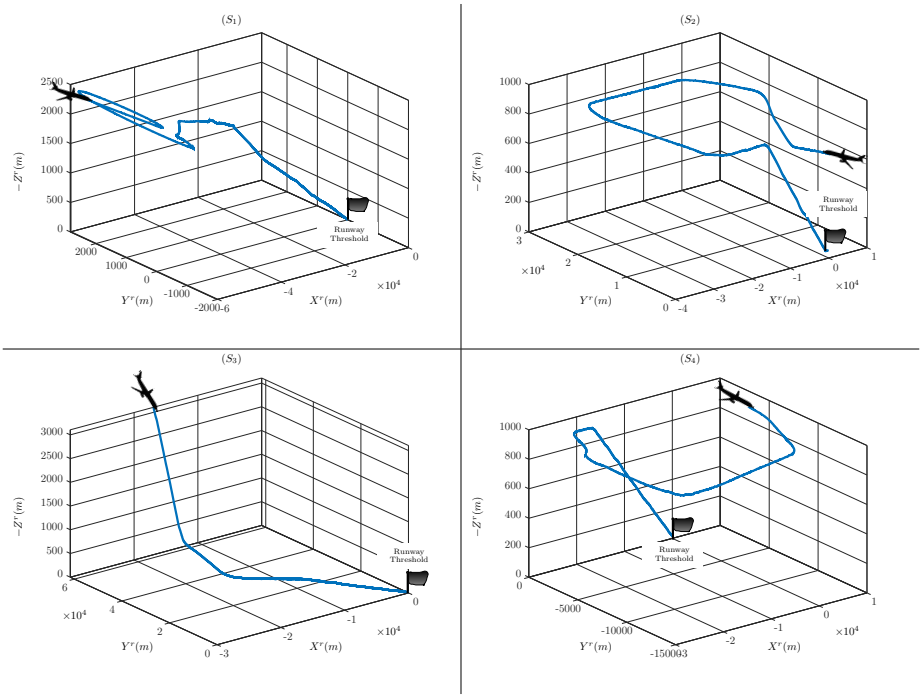

Figure 11: 3D landing trajectories.

The value of the parameter a_{ij} is set to 0.1, $\forall i$ and $\forall j$. This value is directly specified from the desired decay time of the filter and chosen to provide a trade-off between signals smoothing and delaying. IRS, GPS and ILS noise magnitude parameters, f_0, f_1 and f_2, are computed following the procedure described in Subsection 3.2 and are given by: $f_0 = \begin{bmatrix} 0.1087 & 0.4052 & 0.1589 \end{bmatrix}^T$, $f_1 = \begin{bmatrix} 63.3618 & 35.5192 & 4.1909 \end{bmatrix}^T$ and $f_2 = \begin{bmatrix} 0.1625 & 6.3898 \end{bmatrix}^T$. The structure of the ILS pre-filter is based on a simplest low-pass filter described by the following transfer function

$$H(z) = \frac{\beta z^{-1}}{1 + (\beta - 1)z^{-1}} \tag{35}$$

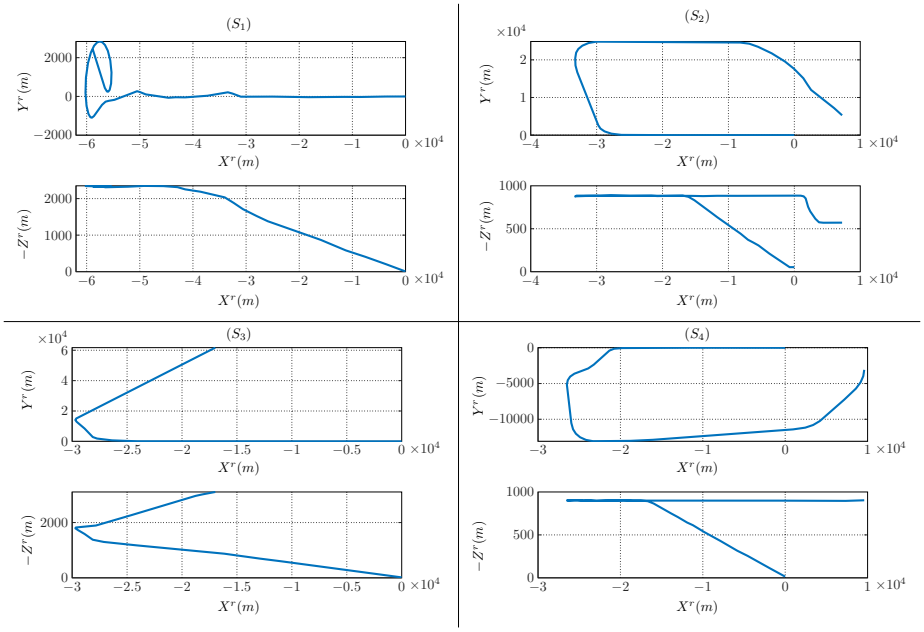

Figure 12: Landing trajectories in x-y and x-z planes.

where β sets the filter cutoff frequency (a value between 0 and 1). This parameter, as well as the Lipschitz constants in (23), the detection thresholds and the moving window length, have been empirically determined using fault-free historical data. The objective is to achieve a good robustness (i.e. avoiding false alarms) of the fault diagnosis scheme while preserving sensitivity to faults. By selecting $\kappa = 2$, the time-covariance matrices Q_0, R_1 and R_2 are updated in real-time. The covariance matrix Q_b is obtained from a diagonal matrix E_b whose diagonal elements are set to 0.01.

In order to evaluate the proposed fault-tolerant data fusion architecture, we first present the data fusion results in the case of nominal behavior of the GPS and ILS sensor groups. To compare with the reference trajectory, recording during the landing scenarios by DGPS (Differential GPS), the absolute position errors of each axis are computed. Figures 13, 14, 15 and 16 illustrate their temporal evolution. In these Figures, LOC and GS validity indices, in the fault-free case, are also presented. In order to quantify the results, the mean absolute error

(MAE) and Standard Deviation (STD) of the position estimates are calculated with respect to DGPS and reported in Table 1. It is shown that reasonable MAEs, less that $10m$, as well as a low STDs are obtained in all evaluated flight data sets. Note that, the observed errors in the position estimation could be due to the initial misalignment between the GPS and DGPS. However, although the resulted accuracy does not perfectly match that of DGPS, the proposed architecture provides, a relevant 3D position estimate. It constitutes therefore a good basis for future studies, namely, the inclusion of more complementary positioning technologies.

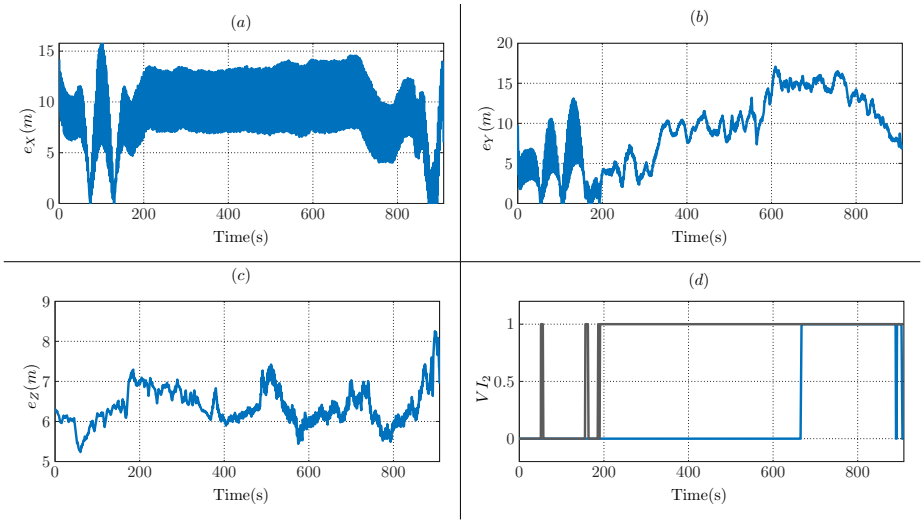

Figure 13: Scenario 1 - Absolute Position errors along x-axis (a), y-axis (b) and z-axis (c); Validity index of GS (blue line) and LOC (gray line) in fault-free case (d).

In a second step, the detection performance in case of fault situations is tested. A set of six additive failure modes were selected for simulation. The first situation corresponds to an additive Gaussian noise with standard deviation $\sigma_f = 8$, added to a constant bias of magnitude $A_f = 20m$. This external signal fault is injected into GPS longitudinal position output at time $t_i = 800s$ and simulates any kind of outside effects. Figure 17 shows the faulty GPS position output and the corresponding validity index. The fault persists for $\Delta T = 30s$

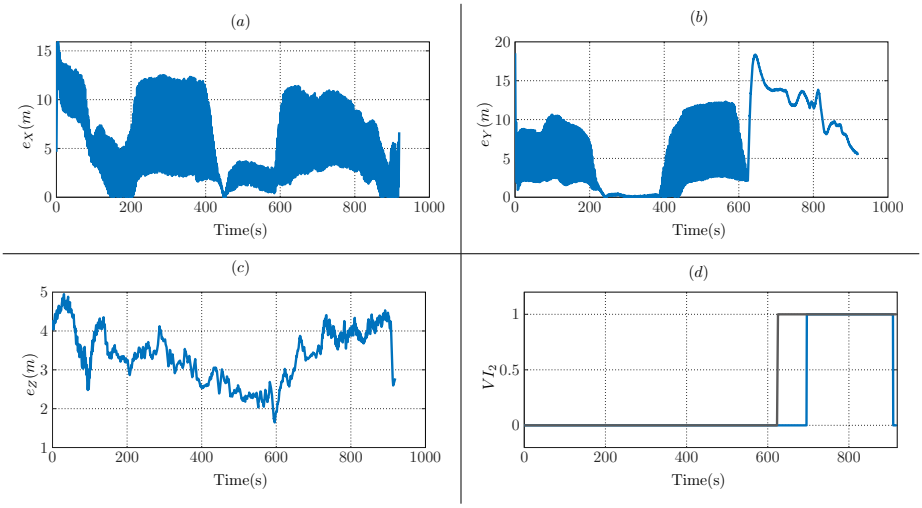

Figure 14: Scenario 2 - Absolute Position errors along x-axis (a), y-axis (b) and z-axis (c); Validity index of GS (blue line) and LOC (gray line) in fault-free case (d).

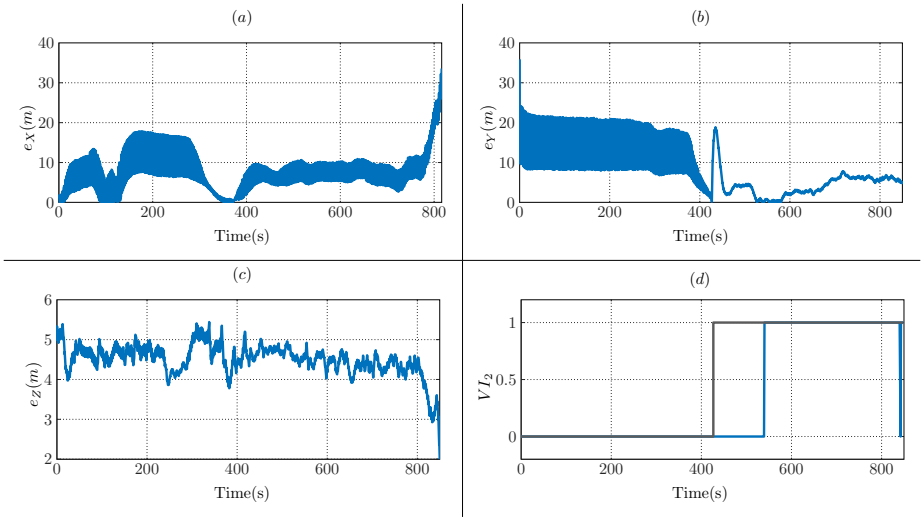

Figure 15: Scenario 3 - Absolute Position errors along x-axis (a), y-axis (b) and z-axis (c); Validity index of GS (blue line) and LOC (gray line) in fault-free case (d).

and the detection time delay is $t_d = 0.2s$.

The second failure is simulated by an additional oscillatory input, exhibiting GPS multipath. This type of external fault can be caused by the reception

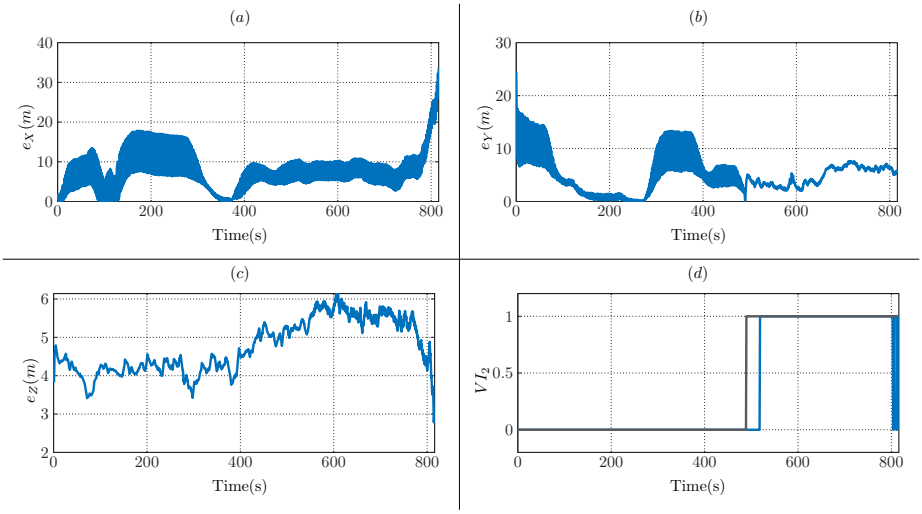

Figure 16: Scenario 4 - Absolute Position errors along x-axis (a), y-axis (b) and z-axis (c); Validity index of GS (blue line) and LOC (gray line) in fault-free case (d).

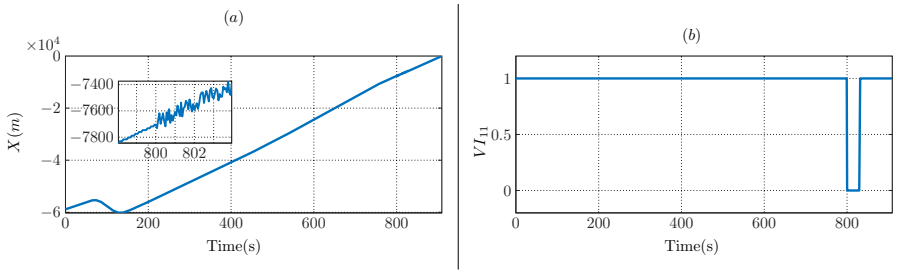

Figure 17: Scenario 1 - Faulty GPS longitudinal position output (a) with its validity index (b).

of additive signals arrived not only from satellites, but also from diffracted or reflected objects. In this scenario, a sinusoidal signal with uniform amplitude $A_f = 60m$ and frequency equal to $4Hz$ is injected at time $t_i = 700s$. The validity indicator becomes active at time instant $t_d = 700.6s$ (See Figure 18).

The third configuration simulates total loss of GPS signal. This type of configuration can be caused by GPS satellites jamming. A noisy mean value jump affecting GPS position in three directions is introduced. The start time of fault injection is $700s$. The time duration of the fault is 20 seconds and is detected

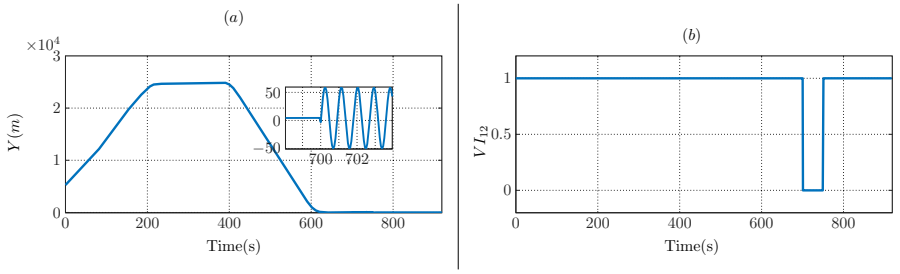

Figure 18: Scenario 2 - Faulty GPS lateral position output (a) with its validity index (b).

with time delay equal to $0.1s$ in all directions. The affected GPS position as well as the corresponding validity indices are shown in the Figure 19.

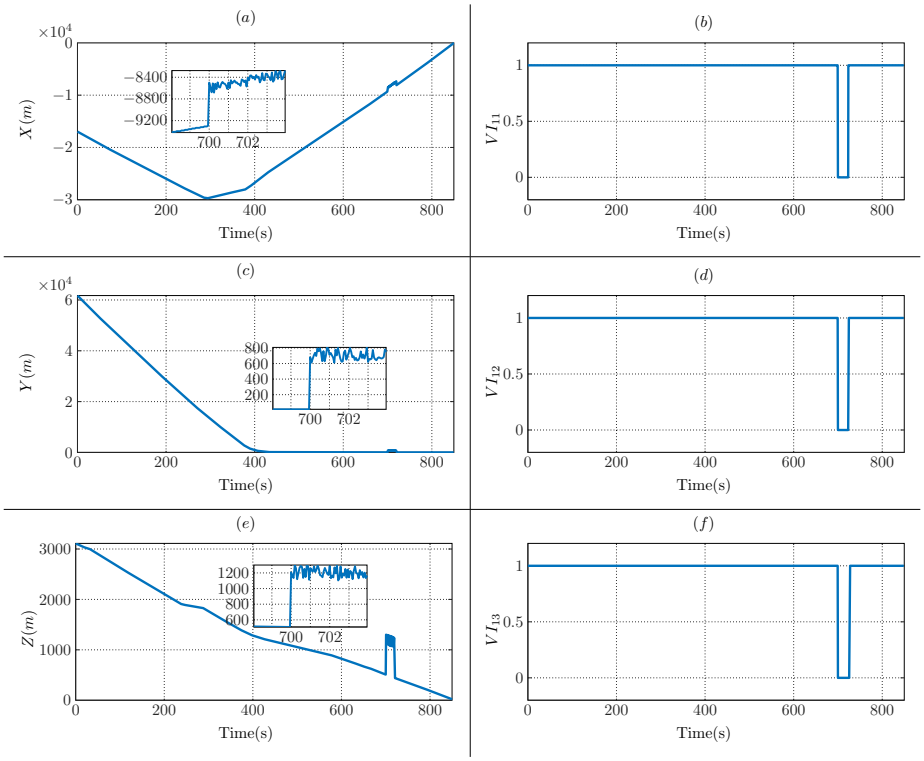

Figure 19: Scenario 2 - Faulty GPS position output in the three directions (a), (c) and (e) with their validity index (b), (d) and (f) .

375 The fourth injected failure is simulated by an additional ramp (see Figure 20-

(a)), representing a Glideslope degenerating sensor. The drift slope is set to $0.05DDM/s$ $(= 0.18°/s)$. The fault is injected at time instant $t_i = 650s$ and persists during $\Delta T = 50s$ (see Figure 20-(b)). The time detection delay is $t_d = 0.8s$.

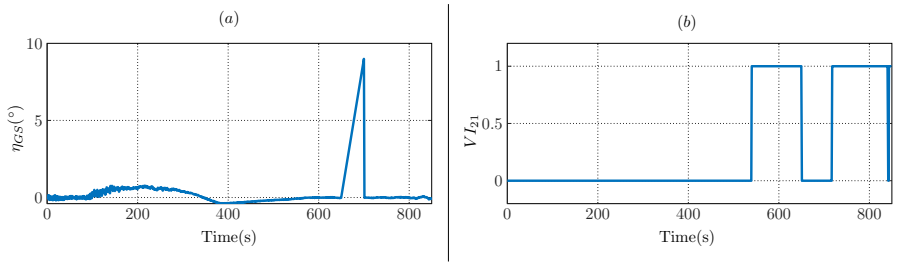

Figure 20: Scenario 3 - Faulty GS deviation output (a) with its validity index (b).

The next considered failures simulate ILS multipath disturbances. Such disturbances occur when the radio signals reaching the aircraft are distorted due to the movement of large metal objects in the radiation area of the transmitter, for instance when an aircraft is taxiing or flying near the runway or when a truck is entering the sensitive area of the ILS. The injected fault affecting the Glideslope deviation measurement is simulated by an additive sinusoidal input with amplitude equal to $A_f = 2DDM = 1.8°$ and frequency equal to $f_f = 2Hz$ (See Figure 21 - (a)). The fault is injected at the time instant $t_i = 700s$ and detected within a time delay equal to $t_d = 0.2s$ (See Figure 21 - (b)).

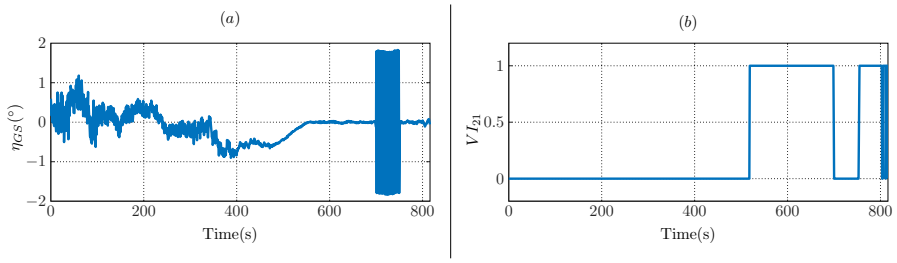

Figure 21: Scenario 4 - Faulty GS deviation output (a) with its validity index (b).

The last failure affects the Localizer and is modeled as an additive sinusoidal entry with non-uniform amplitude. The maximum amplitude and signal fre-

quency are set to $A_f = 2DDM = 483.5\mu A$ and $f_f = 4Hz$, respectively (See Figure 22 - (a)). The fault detection delay is equal to $t_d = 0.1s$ (See Figure 22 - (b)).

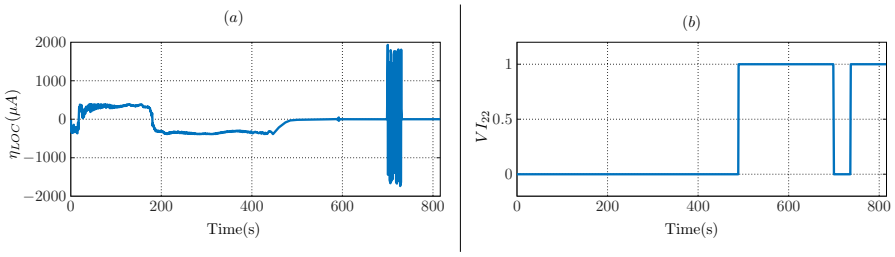

Figure 22: Scenario 4 - Faulty LOC deviation output (a) with its validity index (b).

From previous simulations, it can be concluded that the proposed monitoring layer detects the occurrence of different types of faults, affecting GPS and ILS, with small time detection delay (detection time $\leq 0.8s$) and without false alarms. In terms of estimation accuracy, Table 2 lists the (MAEs) and (STDs) after faulty sensor exclusion. As it can be observed, the estimation errors are almost unchanged. The direct reason for this observation is the rapidity of fault detection which allows to isolate, early in time, the faulty measurements before impacting the accuracy of the data fusion output.

5. Conclusion

This paper has presented a general architecture for fault-tolerant multi-sensor data fusion for aircraft navigation during approach and landing. The paper focused on the data fusion of IRS, GPS and ILS sensors groups with high fault-tolerance capability. Yet, the layered architecture and the modular structure of the proposed scheme allow for easy integration of other type of information sources for reliable aircraft navigation. Simulation experiments based on real flight data provided by Airbus were presented for evaluating the effectiveness of the proposed architecture. Further investigation are needed to validate this scheme on Airbus test facilities using other sensors and in non-

standard and extreme scenarios in order to pave the way for future SPO. This is a topic of our current work.

Acknowledgement

This research has been carried out with financial support provided by the French General Directorate of Civil Aviation (DGAC).

Appendix A. Coordinate Transformations

The different coordinate transformations that are used throughout this paper are summarized in this section.

Conversion From o-frame to e-frame Coordinate Systems [31]. The position vector transformation from the geodetic system to the ECEF coordinate system can be performed using equations (A.2). Given a point in the geodetic system,

$$P^o = \begin{bmatrix} \phi \\ \lambda \\ h \end{bmatrix} \tag{A.1}$$

where ϕ, λ and h, represent latitude, longitude and height above ellipsoid (in meters). The coordinate of P^o in the ECEF frame is given by $P^e = \begin{bmatrix} X^e & Y^e & Z^e \end{bmatrix}^T$, with

$$X^e = \left(\frac{a_e}{\sqrt{1 - e^2 sin^2(\phi)}} + h \right) cos(\phi) cos(\lambda) \tag{A.2a}$$

$$Y^e = \left(\frac{a_e}{\sqrt{1 - e^2 sin^2(\phi)}} + h \right) cos(\phi) sin(\lambda) \tag{A.2b}$$

$$Z^e = \left(\frac{a_e(1 - e^2)}{\sqrt{1 - e^2 sin^2(\phi)}} + h \right) sin(\phi) \tag{A.2c}$$

with a_e and e being the Earth semi-major axis and the eccentricity [3], respectively. These parameters are associated with the WGS84 ellipsoid model. More specifically, we have [32]:

- Semi-major axis: $a_e = 6378137.0m$;
- Flattening factor: $f_e = \frac{1}{298.257223563}$;
- Semi-minor axis: $b_e = a_e(1 - f_e) = 6356752.0m$;
- First eccentricity: $e = \frac{\sqrt{a_e^2 - b_e^2}}{a_e} = 0.08181919$.

Conversion from e-frame to u-frame Coordinate Systems. Since the local navigation frame, i.e u-frame, typically has a different orientation than the e-frame and its origin is typically not located at the earth's center (See Figure A.23), conversion from the e-frame to u-frame requires both a rotation and a translation. More specifically, we have [31]

$$P^u = C_e^u(P^e - P_{O_r}) \tag{A.3}$$

where P_{O_r} is the position of the local runway navigation frame origin in the ECEF coordinate system, and C_e^u is the direction cosine matrix from e-frame to u-frame, which is given by

$$C_e^u = \begin{bmatrix} -sin(\lambda_{RWY}) & cos(\lambda_{RWY}) & 0 \\ -sin(\phi_{RWY})cos(\lambda_{RWY}) & -sin(\phi_{RWY})sin(\lambda_{RWY}) & cos(\phi_{RWY}) \\ cos(\phi_{RWY})cos(\lambda_{RWY}) & cos(\phi_{RWY})sin(\lambda_{RWY}) & sin(\phi_{RWY}) \end{bmatrix} \tag{A.4}$$

where λ_{RWY} and ϕ_{RWY} are the geodetic longitude and latitude corresponding to P_{O_r}.

Conversion from u-frame to r-frame Coordinate Systems. Assume a flat runway with a slope or gradient[4] β_{RWY} from the horizontal plane and an approach direction QFU from the North. Then, as shown in Figure A.24, the

[3] A measure of how much the Earth deviates from being spherical.

[4] The slope of a runway, or gradient, is the difference in elevation from the beginning to the ending of the runway.

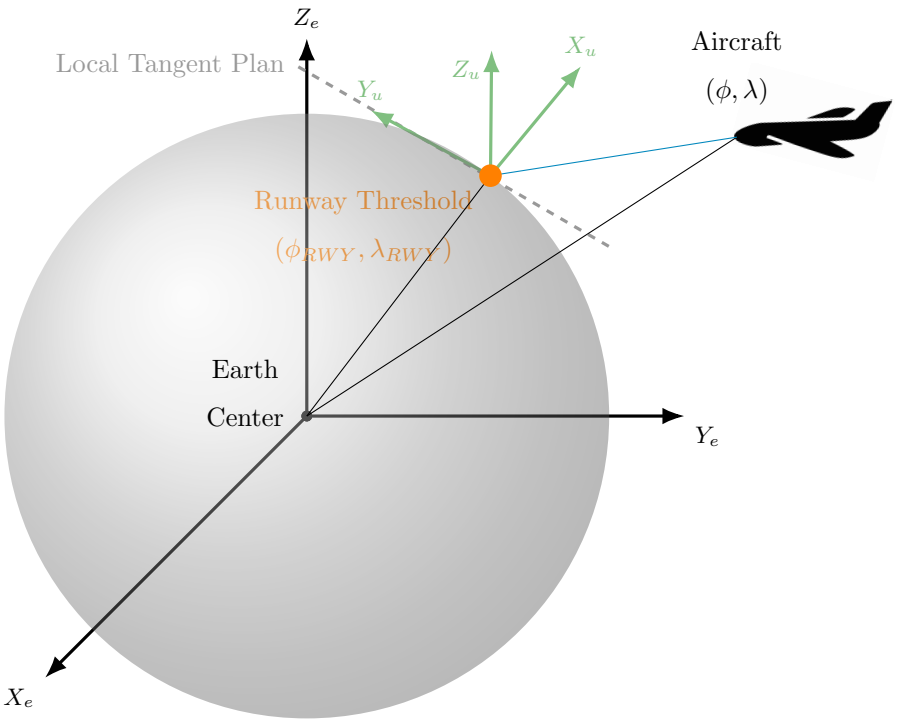

Figure A.23: Illustration of e-frame and u-frame.

runway orientation is taken into account by using the transformation matrix $R_x(\beta_{RWY})\, R_z(QFU)$, afterwards, a transformation from ENU to NWD is applied,

$$C_u^r = \begin{bmatrix} 0 & 1 & 0 \\ -1 & 0 & 0 \\ 0 & 0 & -1 \end{bmatrix} \begin{bmatrix} cos(\beta_{RWY})cos(QFU) & -cos(\beta_{RWY})sin(QFU) & sin(\beta_{RWY}) \\ sin(QFU) & cos(QFU) & 0 \\ -sin(\beta_{RWY})cos(QFU) & sin(\beta_{RWY})sin(QFU) & cos(\beta_{RWY}) \end{bmatrix} \tag{A.5}$$

Then, a point given by P^u in u-frame can be expressed in the runway fixed frame as follows:

$$P^r = C_u^r P^u \tag{A.6}$$

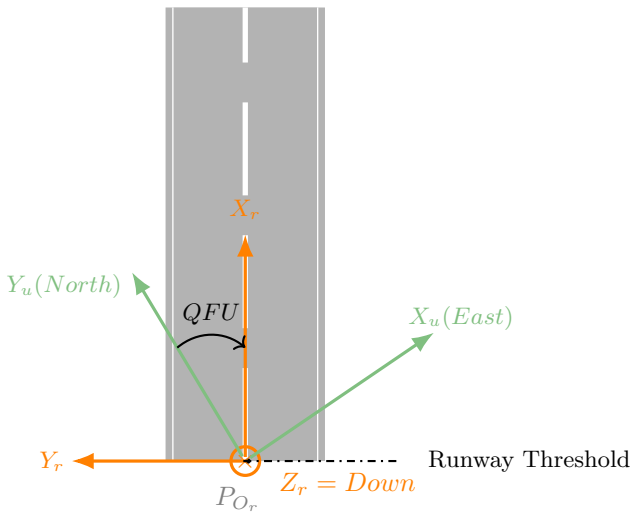

Figure A.24: Illustration of u-frame and r-frame.

References

[1] R. E. Bailey, L. J. Kramer, K. D. Kennedy, C. L. Stephens, T. J. Etherington, An assessment of reduced crew and single pilot operations in commercial transport aircraft operations, in: 2017 IEEE/AIAA 36th Digital Avionics Systems Conference (DASC), IEEE, 2017, pp. 1–15.

[2] M. L. Cummings, A. Stimpson, M. Clamann, Functional requirements for onboard intelligent automation in single pilot operations, in: AIAA Infotech@ Aerospace, 2016, p. 1652.

[3] A. Zolghadri, On flight operational issues management: Past, present and future, Annual Reviews in Control 45 (2018) 41–51.

[4] N. Zhu, J. Marais, D. Bétaille, M. Berbineau, Gnss position integrity in urban environments: A review of literature, IEEE Transactions on Intelligent Transportation Systems 19 (9) (2018) 2762–2778.

[5] O. Petrovska, U. Rechkoska-Shikoska, Aircraft precision landing using integrated GPS/ins system, Transport Problems 8.

[6] G. Wang, X. Xu, Y. Yao, J. Tong, A novel BPNN-based method to overcome the GPS outages for INS/GPS system, IEEE Access 7 (2019) 82134–82143.

[7] J. Lee, M. Kim, Optimized GNSS station selection to support long-term monitoring of ionospheric anomalies for aircraft landing systems, IEEE Transactions on Aerospace and Electronic Systems 53 (1) (2017) 236–246.

[8] Z. Yue, B. Lian, C. Tang, K. Tong, A novel adaptive federated filter for GNSS/INS/VO integrated navigation system, Measurement Science and Technology 31 (8) (2020) 085102.

[9] Y. Watanabe, A. Manecy, A. Hiba, S. Nagai, S. Aoki, Vision-integrated navigation system for aircraft final approach in case of GNSS/SBAS or ILS failures, in: AIAA Scitech 2019 Forum, 2019, p. 0113.

[10] V. Gibert, F. Plestan, L. Burlion, J. Boada-Bauxell, A. Chriette, Visual estimation of deviations for the civil aircraft landing, Control Engineering Practice 75 (2018) 17–25.

[11] W. Hundley, S. Rowson, G. Courtney, V. Wullschleger, R. Velez, P. O'DONNELL, Flight evaluation of a basic C/A-code differential GPS landing system for category I precision approach, Navigation 40 (2) (1993) 161–178.

[12] M. K. Al-Sharman, B. J. Emran, M. A. Jaradat, H. Najjaran, R. Al-Husari, Y. Zweiri, Precision landing using an adaptive fuzzy multi-sensor data fusion architecture, Applied soft computing 69 (2018) 149–164.

[13] C. Xu, X. Huang, M. Li, D. Wang, Landmark database selection for vision-aided inertial navigation in planetary landing missions, Aerospace Science and Technology (2021) 107040.

[14] L. Zhang, Z. Zhai, L. He, P. Wen, W. Niu, Infrared-inertial navigation for commercial aircraft precision landing in low visibility and gps-denied environments, Sensors 19 (2) (2019) 408.

[15] A. Hiba, A. Gáti, A. Manecy, Optical navigation sensor for runway relative positioning of aircraft during final approach, Sensors 21 (6) (2021) 2203.

[16] K. Kolosov, A. Miller, B. Miller, Robust data fusion of uav navigation measurements with application to the landing system, Remote Sensing 12 (23) (2020) 3849.

[17] A. Videmsek, M. U. de Haag, T. Bleakley, Evaluation of radar altimeter-aided gps for precision approach using flight test data, in: 2019 IEEE/AIAA 38th Digital Avionics Systems Conference (DASC), IEEE, 2019, pp. 1–10.

[18] R. E. Kalman, et al., Contributions to the theory of optimal control, Bol. soc. mat. mexicana 5 (2) (1960) 102–119.

[19] S. Yazdkhasti, J. Z. Sasiadek, Multi sensor fusion based on adaptive kalman filtering, in: Advances in Aerospace Guidance, Navigation and Control, Springer, 2018, pp. 317–333.

[20] S. Ifqir, C. Combastel, A. Zolghadri, G. Alcalay, P. Goupil, S. Merlet, A fault-tolerant data fusion scheme for integrated navigation in civil aviation operations, 19th European Control Conference, 2021.

[21] A. Zolghadri, A redundancy-based strategy for safety management in a modern civil aircraft, Control Engineering Practice 8 (5) (2000) 545–554.

[22] D. of Defense, World geodetic system 1984, National Imagery and Mapping Agency.

[23] C. Combastel, Zonotopes and kalman observers: Gain optimality under distinct uncertainty paradigms and robust convergence, Automatica 55 (2015) 265–273.

[24] C. Combastel, An extended zonotopic and gaussian kalman filter (EZGKF) merging set-membership and stochastic paradigms: Toward non-linear filtering and fault detection, Annual Reviews in Control 42 (2016) 232–243.

[25] D. McCollum, Evaluation of instrument landing system DDM calibration accuracies, Master's thesis, Faculty of the School of Engineering of the Air Force Institute of Technology Air University (December 1983).

[26] A. Levant, Robust exact differentiation via sliding mode technique, automatica 34 (3) (1998) 379–384.

[27] A. Varga, D. Ossmann, Lpv-model based identification approach of oscillatory failure cases, IFAC Proceedings Volumes 45 (20) (2012) 1347–1352.

[28] G. Minkler, J. Minkler, Theory and applications of Kalman filtering, Magellan Book Company, 1993.

[29] M. NøRgaard, N. K. Poulsen, O. Ravn, New developments in state estimation for nonlinear systems, Automatica 36 (11) (2000) 1627–1638.

[30] C. Sun, Y. Zhang, G. Wang, W. Gao, A maximum correntropy divided difference filter for cooperative localization, IEEE Access 6 (2018) 41720–41727.

[31] A. Noureldin, T. B. Karamat, J. Georgy, Fundamentals of inertial navigation, satellite-based positioning and their integration, Springer Science & Business Media, 2012.

[32] G. Cai, B. M. Chen, T. H. Lee, Unmanned rotorcraft systems, Springer Science & Business Media, 2011.

Algorithm 1: Confidence Interval Computation Algorithm

Function `IntervalPredictor`$(c_{ij}[k], r_{ij}[k], y^r_{ij}[k], a_{ij}, f_{ij})$

if $r_{ij}[k] < f_{ij}$ **then**
  $\gamma_{ij}[k] = a_{ij}$;
else
  $\gamma_{ij}[k] = 0$;
endif

$c_{ij}[k+1] = \gamma_{ij}[k]c_{ij}[k] + (1 - \gamma_{ij}[k])y^r_{ij}[k]$;

$r_{ij}[k+1] = pos(|y^r_{ij}[k] - c_{ij}[k]| - f_{ij}) + a_{ij}.min(r_{ij}[k], f_{ij})$;

$$\begin{aligned}
\overline{x}^r_{ij}[k] &= c_{ij}[k] + r_{ij}[k]; \\
\underline{x}^r_{ij}[k] &= c_{ij}[k] - r_{ij}[k]; \\
\overline{y}^r_{ij}[k] &= \overline{x}^r_{ij}[k] + f_{ij}; \\
\underline{y}^r_{ij}[k] &= \underline{x}^r_{ij}[k] - f_{ij};
\end{aligned}$$

return $(c_{ij}[k+1], r_{ij}[k+1])$

Function `Main`

for $k = 1$ **to** N **do**
  for $i = 1$ **to** m **do**
    for $j = 1$ **to** m_i **do**
      $[c_{ij}[k+1], r_{ij}[k+1]] =$
        `IntervalPredictor`$(c_{ij}[k], r_{ij}[k], y^r_{ij}[k], a_{ij}, f_{ij})$

return $(c_{ij}[k+1], r_{ij}[k+1])$

Algorithm 2: Global Fusion Algorithm

Inputs: $\hat{\tilde{x}}^r[k]$, $P[k]$, $c_0[k]$, $y^r[k]$;

Update:

$$K[k] = \left(P^{(p)}[k]\ H^T[k]\ \left(H[k]\ P^{(p)}[k]\ H^T[k] + R[k]\right)^{-1}\right) S[k]\ ;$$

$$\hat{\tilde{x}}^r[k] = \tilde{x}^{(p)}[k] + K[k]\left(y^r[k] - h(\tilde{x}^{(p)}[k])\right)\ ;$$

$$P[k] = (I - K[k]\ H[k])P^{(p)}[k];$$

Predict:

$$\tilde{x}^{(p)}[k+1] = \tilde{A}_0\ \hat{\tilde{x}}^r[k] + \tilde{B}_0\ c_0[k];$$

$$P^{(p)}[k+1] = \tilde{A}_0\ P[k]\ \tilde{A}_0^T + Q_0[k];$$

Outputs: $\hat{\tilde{x}}^r[k+1]$ and $P[k+1]$;

	MAE (m)			STD (m)		
	x-axis	y-axis	z-axis	x-axis	y-axis	z-axis
Scenario 1	9.0479	9.0829	6.3706	2.8107	4.3669	0.4669
Scenario 2	5.3864	6.6069	3.3539	3.3539	4.8517	0.6828
Scenario 3	6.0580	8.9551	4.5070	4.2321	6.1857	0.3833
Scenario 4	7.7401	5.0160	4.7327	4.4922	3.3615	0.6866

Table 1: MAEs and STDs of the position errors along x-, y- and z-axis.

	MAE (m)			STD (m)		
	x-axis	y-axis	z-axis	x-axis	y-axis	z-axis
Scenario 1 (fault along GPS x-axis)	9.1675	9.0829	6.3706	2.9721	4.3672	0.4677
Scenario 2 (fault along GPS y-axis)	5.3882	6.8450	3.3566	3.3548	5.2848	0.6828
Scenario 3 (Complete loss of GPS)	6.0832	8.9796	4.5211	4.2608	6.2902	0.3890
Scenario 3 (GS fault)	6.0580	8.9551	4.5070	4.2186	6.1857	0.3817
Scenario 4 (GS fault)	7.7685	5.0162	4.7301	4.4792	3.3615	0.6828
Scenario 4 (LOC fault)	7.7367	4.7942	4.7329	4.4919	3.4210	0.6866

Table 2: MAEs and STDs of the position errors along x-, y- and z-axis in fault occurrence case.